

E^2 distribution and statistical regularity in polygonal planar tessellations

Ran Li¹, Consuelo Ibar², Zhenru Zhou², Seyedsajad Moazzeni¹,
Kenneth D. Irvine^{2*}, Liping Liu^{1,3†}, and Hao Lin^{1‡}

November 9, 2020

1. Department of Mechanical and Aerospace Engineering, Rutgers, The State University of New Jersey
2. Waksman Institute and Department of Molecular Biology and Biochemistry, Rutgers, The State University of New Jersey
3. Department of Mathematics, Rutgers, The State University of New Jersey

Abstract

From solar supergranulation to salt flat in Bolivia, from veins on leaves to cells on *Drosophila* wing discs, polygon-based networks exhibit great complexities, yet similarities persist and statistical distributions can be remarkably consistent. Based on analysis of 99 polygonal tessellations of a wide variety of physical origins, this work demonstrates the ubiquity of an exponential distribution in the squared norm of the deformation tensor, E^2 , which directly leads to the ubiquitous presence of Gamma distributions in polygon aspect ratio. The E^2 distribution in turn arises as a χ^2 -distribution, and an analytical framework is developed to compute its statistics. E^2 is closely related to many energy forms, and its Boltzmann-like feature allows the definition of a pseudo-temperature. Together with normality in other key variables such as vertex displacement, this work reveals regularities universally present in all systems alike.

Polygonal networks are one of nature’s favorite ways of organizing the multitude - from supergranulation on the solar surface [29] to cracked dry earth [37]; from ice wedges in northern Canada [61] to the scenic Salar de Uyuni in Bolivia [23]; and from veins on leaves [11] to cells on *Drosophila* wing discs [53] (Fig. 1). These systems are driven by distinctive physical mechanisms, yet they share common features. Individual constituents, namely, “cells” appear to “randomize” into statistical distributions, and only interact with their immediate neighbors. On the collective level, especially in the dynamic and active systems, rich phenomena are observed, including unjamming and jamming, fluid-to-solid phase transition, and flow and migration [7, 19, 22, 34, 42, 50, 54, 63, 68].

Despite the complexity and variabilities involved in these phenomena, similarity patterns emerge. One particularly interesting instance is provided recently by Atia *et al.* [3]. Within the context of confluent biological tissue and based on extensive experiments both *in vitro* and *in vivo*, the authors found that data

*Corresponding email: irvine@waksman.rutgers.edu

†Corresponding email: liu.liping@rutgers.edu

‡Corresponding email: hlin@soe.rutgers.edu

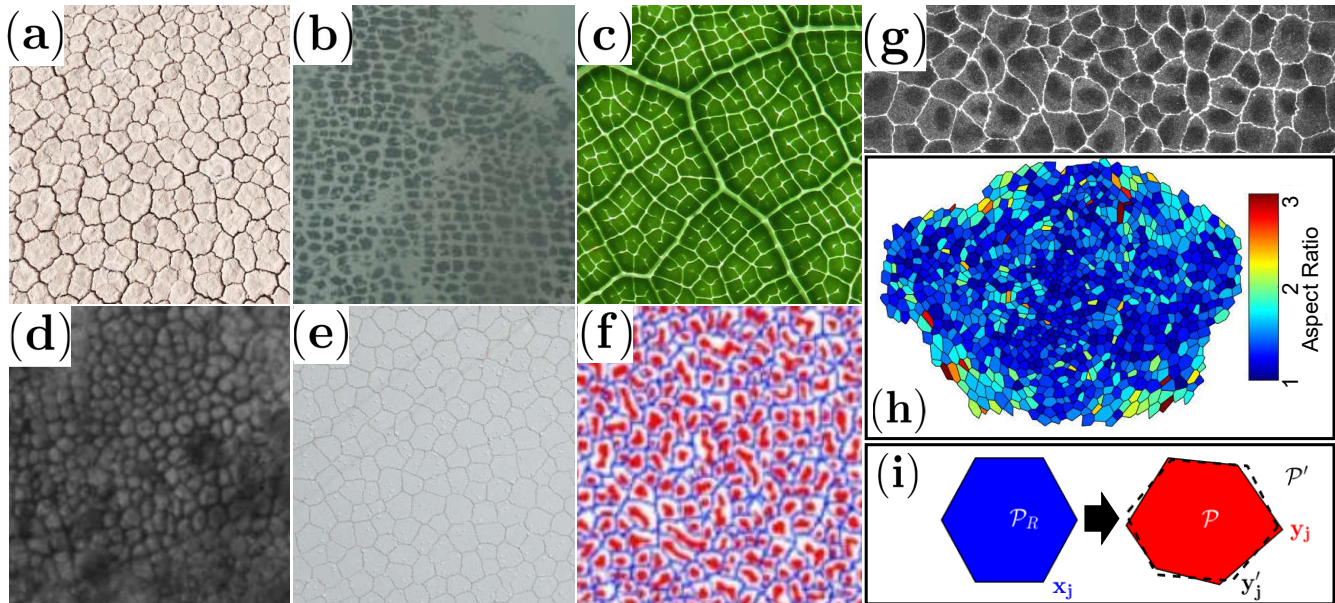


Figure 1: (a)-(h) Examples of randomized polygonal networks in nature. (a) Land cracks due to desiccation [37]; (b) Ice wedges from northern Canada [61]; (c) Veins on a *Ficus lyrata* leaf [11]; (d) Desiccation pattern of an ancient lake on Mars [43]; (e) A snapshot of Salar de Uyuni in Bolivia, world’s largest salt flat [23]; (f) Supergranulation on solar surface [29]; (g) Plated MDCK cells (this work). (h) A processed image of a developing *Drosophila* wing disc (this work) with the aspect ratio of cells color-mapped. (i) A regular hexagon \mathcal{P}_R (blue, with vertices \mathbf{x}_j), a deformed hexagon \mathcal{P} (red, with vertices \mathbf{y}_j), and a uniform deformation as mean-field approximation \mathcal{P}' (black dashed outline, with vertices \mathbf{y}'_j).

on cell aspect ratio collapse and follow a normalized Gamma distribution, implying a universal principle underlying the geometric configuration and pertinent processes.

What is the basis of this universality? Does it carry beyond the biological context? This work composes of a two-part discovery to answer these questions. In the first, we analyze a total of 99 data sets in 8 groups that include convection patterns (solar supergranulation), landforms (salt flats, on Mars, and in or near the Arctic), cracked dry earth, and biological patterns (veins on leaves, cells on *Drosophila* wing discs, and plated MDCK cells). (Fig. 1 and Table 1.) We demonstrate that the Gamma distribution in polygon aspect ratio derives from an exponential distribution in the squared strain tensor norm, E^2 , based on which we develop a unifying solution for the former. Both distributions persist in all data examined. In the second, we tackle the origin of the E^2 distribution, and demonstrate that it arises as a χ^2 -distribution owing to asymptotic normality of vertex displacement and other key variables. We present a theoretical framework to accurately compute E^2 from vertex statistics. Importantly, E^2 is closely related to various definitions of system energy including all of the bulk-, perimeter-, and moment-based (known as the Quantizer) forms [7, 15, 27, 34, 36, 44]. The Boltzmann-like feature of E^2 enables the definition of a pseudo-temperature that can be considered as a consistent quantifier [4, 17, 18, 47]. The exponential and normal distributions we reveal in this work are hidden regularities that transcend the specific physical systems, and are embedded universal features of random polygonal tessellations.

\mathbf{E}^2 and its relationship with aspect ratio

In this first part of this work, we define \mathbf{E}^2 and analytically establish its relationship with the polygon aspect ratio. We demonstrate that a k -Gamma distribution in the latter is derivable from an exponential distribution in the former. We begin by defining the mean-field deformation tensor, \mathbf{E} . An exemplary processed image of a *Drosophila* wing disc 120h after egg laying (AEL) is shown in Figure 1h, where the color scale indicates magnitude of the cell aspect ratio (defined in Methods). We choose as our reference frame a *regular* n -polygon centered at the origin, with vertices

$$\mathbf{x}_j = r_0 \mathbf{e}_j, \quad \mathbf{e}_j = [\cos(j2\pi/n), \sin(j2\pi/n)], \quad j = 1, \dots, n. \quad (1)$$

This polygon is denoted by \mathcal{P}_R , and r_0 is a scaling factor. Figure 1k uses $n = 6$, a hexagon as an illustrative example. We consequently regard any n -sided polygon \mathcal{P} with vertices \mathbf{y}_j as a “deformation” from \mathcal{P}_R ,

$$\mathbf{y}_j = \mathbf{x}_j + \mathbf{u}_j, \quad j = 1, \dots, n. \quad (2)$$

Note that this deformation is to be understood as a morphological deviation from the reference \mathcal{P}_R , rather than an actual physical deformation, although the latter is a possibility. We also require that the centroid of \mathcal{P} is aligned with that of \mathcal{P}_R . The deformation is in general non-uniform, in the sense that for $n \geq 3$, a single deformation tensor of $\mathbf{F} \in \mathbb{R}^{2 \times 2}$ cannot be identified by $\mathbf{y}_j = \mathbf{F}\mathbf{x}_j$ for all of $j = 1, \dots, n$. Nevertheless we *can* introduce an approximation, namely,

$$\mathbf{y}_j \approx \mathbf{y}'_j = \mathbf{F}\mathbf{x}_j, \quad j = 1, \dots, n. \quad (3)$$

This approximation is analogous to a Taylor expansion in which only the leading order term is retained. The use of a uniform deformation to approximate the local and non-uniform deformation field is effectively coarse-graining, reducing the degree of freedom from $2n$ to 4 and suppressing the fluctuations. This idea is illustrated in Figure 1i (right), where \mathcal{P}' is the approximate and uniformly deformed polygon. From \mathbf{F} we define the usual strain tensor and its squared Frobenius norm,

$$\mathbf{E} = (\mathbf{F}^T \mathbf{F})^{\frac{1}{2}} - \mathbf{I} \approx \frac{1}{2}[(\mathbf{F} - \mathbf{I}) + (\mathbf{F} - \mathbf{I})^T], \quad |\mathbf{E}|^2 = \text{Tr}(\mathbf{E}^T \mathbf{E}), \quad (4)$$

where \mathbf{I} is the identity tensor, and the approximation in the first equation is valid in the small-to-moderate deformation regime. In this work we use $|\mathbf{E}|^2$ (mathematical representation) and \mathbf{E}^2 (terminology) interchangeably. The restriction to isochoric (area-conserved) deformation requires that $\det \mathbf{F} = 1$ and equivalently (to leading order), $\text{Tr} \mathbf{E} = 0$, which is satisfied by choosing r_0 in (1). Consequently, \mathbf{E} has a small degree of freedom of 2, which eventually leads to its strong regularity that we demonstrate later.

We pursue an analytical expression for \mathbf{E} via minimizing the difference between \mathbf{y}_j 's and \mathbf{y}'_j 's in (3), from which we obtain (SI)

$$\mathbf{E} = \frac{1}{n} \sum_{j=1}^n [\mathbf{v}_j \otimes \mathbf{e}_j + \mathbf{e}_j \otimes \mathbf{v}_j - (\mathbf{e}_j \cdot \mathbf{v}_j) \mathbf{I}], \quad (5)$$

$$|\mathbf{E}|^2 = \sum_{i=1}^n \sum_{j=1}^n \mathbf{v}_i \cdot \mathbf{C}_{ij} \mathbf{v}_j, \quad \mathbf{C}_{ij} = \frac{2}{n^2} [(\mathbf{e}_i \cdot \mathbf{e}_j) \mathbf{I} + \mathbf{e}_j \otimes \mathbf{e}_i - \mathbf{e}_i \otimes \mathbf{e}_j]. \quad (6)$$

Here

$$\mathbf{v}_j = \mathbf{u}_j/r_0, \quad r_0 = \frac{1}{n} \sum_{j=1}^n \mathbf{y}_j \cdot \mathbf{e}_j. \quad (7)$$

In addition to satisfying the trace-free condition, the scaling also ensures that \mathbf{v}_j 's are dimensionless. Further details on the computation of $|\mathbf{E}|^2$ is deferred until later. For now we show that if \mathbf{E}^2 follows an exponential distribution (that shall be validated below both via data and analysis), namely,

$$\rho_{\mathbf{E}}(|\mathbf{E}|^2) = \beta \exp(-\beta|\mathbf{E}|^2), \quad (8)$$

then the aspect ratio follows a k -Gamma distribution such as shown in [3]. Here $\rho(\cdot)$ denotes a (normalized) probability density function (PDF), and β is similar to an inverse temperature as the PDF is Boltzmann-like. The aspect ratio a_r of the polygon is calculated via the second area moments (Methods), and is related to \mathbf{E}^2 by (SI)

$$a_r^2 = (x+1)^2 = g(|\mathbf{E}|^2), \quad g(t) = 1 + 2t^2 + 4t + [(2t^2 + 4t + 1)^2 - 1]^{1/2}, \quad (9)$$

where for convenience we define a shape factor x in relation to a_r using $x = a_r - 1$. Based on (8, 9), a transformation $\rho_{\mathbf{E}}(|\mathbf{E}|^2)d|\mathbf{E}|^2 = \rho_X(x)dx$ leads to

$$\rho_X(x) = \rho_{\mathbf{E}}(|\mathbf{E}|^2) \frac{d|\mathbf{E}|^2}{dx} = \beta \zeta'(x) \exp(-\beta \zeta(x)), \quad (10)$$

where

$$\zeta(x) = g^{-1}((x+1)^2).$$

Here we have considered the normalization condition. Equation (10) is our prediction of the distribution in the aspect ratio.

Data validate \mathbf{E}^2 and a_r distributions

Both distributions and their relationship are extensively validated with a total of 99 data sets spanning 8 groups summarized in Table 1; detailed descriptions, data sources, and method of analysis are presented in the Methods section. Figure 2 uses 4 representative cases to demonstrate the agreement. (More are shown in Fig. S2 in the SI.) The left column shows the PDFs of $|\mathbf{E}|^2$, which are very well fitted by the exponential form, $\exp(-\beta|\mathbf{E}|^2)$, where β is extracted as a fitting parameter. (See also Fig. 4b where all $|\mathbf{E}|^2$ profiles are presented and the value of β is theoretically predicted.)

The center column shows the PDFs of the shape factor, $a_r - 1$ (symbols). The theoretical predictions per Eq. (10) are shown in dashed, and exhibit excellent agreement with data. They are generated per Eq. (10), with the single input parameter, β , extracted from the analysis of $|\mathbf{E}|^2$ distribution.

Lastly in the right column, the PDFs for $a_r - 1$ are normalized with $\langle a_r \rangle - 1$, where $\langle \cdot \rangle$ denotes a mean, e.g.,

$$\langle x \rangle = \int_0^\infty x \rho_X(x) dx. \quad (11)$$

Both data and theoretical predictions are normalized following this practice. The dot-dashed are best fits

Type (abbreviation)	M	N	$R^2, \mathbf{E} ^2$	$R^2, a_r - 1$
Salt Flat of Uyuni (Salt Flat)	7	193 – 849	0.994 ± 0.0058	0.939 ± 0.0255
Landforms on Mars (Mars)	9	219 – 5826	0.986 ± 0.0125	0.935 ± 0.0461
Veins on Leaves (Leaves)	6	338 – 6050	0.994 ± 0.0047	0.936 ± 0.0328
Landforms in the Arctic (Arctic)	11	104 – 1061	0.982 ± 0.0169	0.902 ± 0.0728
Supergranulation on Solar Surface (Solar)	9	192 – 1645	0.991 ± 0.0075	0.932 ± 0.0463
Cracked Dry Earth (Cracks)	11	298 – 1596	0.992 ± 0.0067	0.943 ± 0.0353
Drosophila Wing Disc (Droso)	42	902 – 4205	0.991 ± 0.0083	0.955 ± 0.0335
Plated MDCK Cells (MDCK)	4	1148 – 2283	0.997 ± 0.0012	0.936 ± 0.0157

Table 1: Summary of data for a total of $M_{\text{tot}} = 99$ tessellations. Abbreviations are defined within parentheses and are used in figure legends; M is data sets in each type; N , the number of polygons in each set (range provided). R^2 for $|\mathbf{E}|^2$ indicates quality of fitting (e.g., in left column, Fig. 2); R^2 for $a_r - 1$ indicates quality of agreement between theory and data (e.g., in middle column, Fig. 2). Data sources are presented in Methods.

using a k -Gamma distribution defined as

$$\rho_{kG}(x_1; k) = \frac{k^k}{\Gamma(k)} x_1^{k-1} \exp(-kx_1), \quad (12)$$

where $\Gamma(k)$ is the Gamma function, and k is the single fitting parameter. The agreement is evident, and the k -values are found to vary between 2 and 3.

Overall corroboration between theory and data is quantified by the coefficient of determination, R^2 , and are listed in Table 1 for all cases (see Methods for definition). The values are uniformly close to 1 (“perfect agreement”) with minimal variations from case to case. Validity of the theoretical prediction (10) is also attested by Fig. 3a. Here we define a pseudo temperature T as the inverse of β , namely, $T = \beta^{-1}$. To compare with data, a theoretical prediction is generated by using (10) in the integration (11).

The above results validate that the E^2 does follow an exponential, Boltzmann-like distribution. The universality of this distribution in all data sets, according to our theory, necessarily leads to a universality of k -Gamma distributions for the aspect ratio. That is, the validity extends beyond the confluent tissues studied in [3], and to all systems we analyzed. As a corollary, (10) provides a fundamental solution for the aspect ratio, of which the k -Gamma distributions (12) are convenient approximations. This solution does not normalize to a single curve with a single k value if fitted with Gamma distributions. In fact, it predicts a positive correlation between β and k (Fig. S8). Qualitatively, this means that PDFs of aspect ratio (a_r , or equivalently, x) with wider spread and greater mean (corresponding to lower values of β) present themselves relatively to the left after normalization (corresponding to lower values of k and noting that maxima occur at $1 - 1/k$ per (12)). This trend is fully corroborated with data from our own work (Fig. 2, and Fig. S2 in SI, center and right columns) and Atia et al. [3] (Fig. 3 therein), as well as predictions from a self-propelled Voronoi model in the supplemental information of the latter. In summary, the variability in k arises from the variability in β .

We remark that the agreement between our theoretical prediction and data can be even better if we use a variation of the deformation tensor computed as the square-root of the area moment tensor, \mathbf{M} , via Eq. (21) in the Methods section. This is not surprising, as now both \mathbf{E} and a_r share the same origin, the agreement shown in Fig. 3a inset is near perfect. The slight differences between the two definitions are

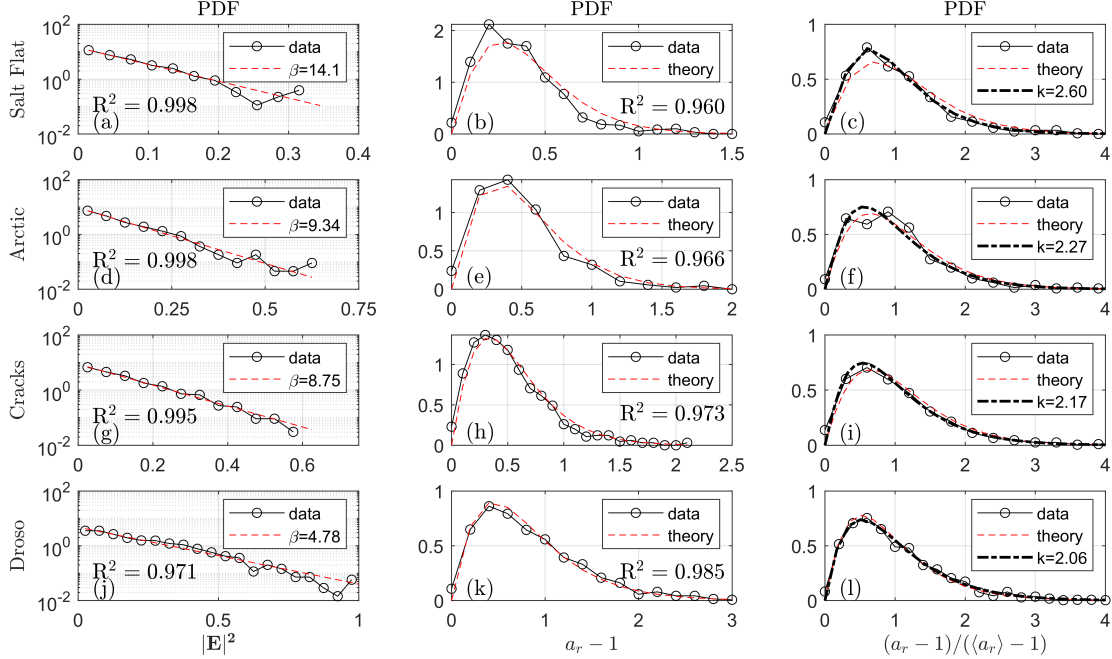


Figure 2: Universality in strain and aspect ratio distributions. Left column shows the PDFs of $|\mathbf{E}|^2$, fitted with an exponential form $\exp(-\beta|\mathbf{E}|^2)$ to extract β . This β value is used in Eq. (10) to generate the theoretical curves in the middle column (dash), in comparison to the aspect ratio data (symbols). The coefficients of determination, R^2 are shown within the panels. Right column: both data and theoretical curves from the center column are normalized using the mean values, and fitted with a k -Gamma function (12) (thick dashed). A single parameter k is extracted and shown in the figure legends. Data are from [21], [2], and [60], respectively, for the top 3 rows; and from this work for Drosos.

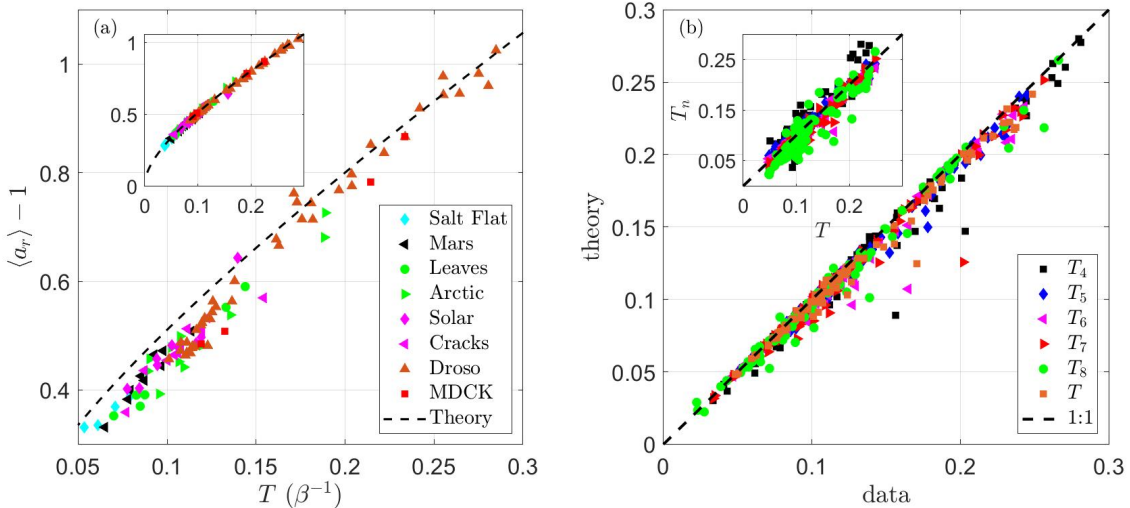


Figure 3: (a) Overall correlation between a_r and $T (\beta^{-1})$ for all 99 data sets (symbols); the theoretical prediction (dashed) is generated per (10). The inset alternatively presents \mathbf{E} from a moment-based calculation which further improves agreement. (b) A comparison between data and predicted temperature, T_n and T (“theory”). The inset shows that sub-ensemble temperature T_n ’s are quantitatively similar to tessellation temperature, T .

due to higher order effects that we theoretically and numerically demonstrate in the SI. Here and below we focus on using (5) for its apparent analytical simplicity.

\mathbf{E}^2 distribution is a χ^2 -distribution

In the second part of this work, we demonstrate the origin of the highly regular statistical distribution in \mathbf{E}^2 . Figure 3b shows results comparing the pseudo-temperature computed from Eq. (6) (denoted “data”) with the theoretical prediction we develop below (denoted “theory”). Here the subscript n denotes a restriction to the sub-ensemble of n -gons, $T_n := \langle |\mathbf{E}|^2 \rangle_n$. Polygons other than $n = 4-8$ are of statistically insignificant occurrences and not included in the evaluation.

The key relationship we utilize is a quadratic form to compute $|\mathbf{E}|^2$ given vertex displacement, \mathbf{v}_j ,

$$|\mathbf{E}|^2 = \hat{\mathbf{v}} \cdot \hat{\mathbf{C}} \hat{\mathbf{v}}. \quad (13)$$

Here $\hat{\mathbf{v}}$ is a concatenated vector in \mathbb{R}^{2n} ,

$$\hat{\mathbf{v}} := \begin{bmatrix} \hat{v}_1 \\ \vdots \\ \hat{v}_{2n} \end{bmatrix} = \begin{bmatrix} \mathbf{v}_1 \\ \vdots \\ \mathbf{v}_n \end{bmatrix}. \quad (14)$$

Other vectors such as $\hat{\mathbf{y}}$, $\hat{\mathbf{u}}$, and $\hat{\mathbf{e}}$ are similarly defined from their two-dimensional counterparts, and all vectors and tensors in the $2n$ -dimensional space are denoted by a hat to differentiate from the planar quantities. $\hat{\mathbf{C}} \in \mathbb{R}_{\text{sym}}^{2n \times 2n}$ is a second-order tensor with block components \mathbf{C}_{ij} given in (6). Not surprisingly, $\hat{\mathbf{C}}$ has 2 non-trivial eigenvalues (SI), matching the degree of freedom of \mathbf{E} (note that $\mathbf{E} = (E_{11}, E_{12}; E_{12}, -E_{11})$ in a general component form):

$$\hat{\mathbf{P}}^T \hat{\mathbf{C}} \hat{\mathbf{P}} = \text{diag}(2/n, 2/n, 0, \dots, 0).$$

The diagonalization above with the orthonormal tensor $\hat{\mathbf{P}}$ helps us express $|\mathbf{E}|^2$ in a particularly simple form,

$$|\mathbf{E}|^2 = \frac{2}{n} (\hat{w}_1^2 + \hat{w}_2^2), \quad \hat{\mathbf{w}} := \hat{\mathbf{P}}^T \hat{\mathbf{v}}. \quad (15)$$

We realize that $\hat{w}_k = \hat{\mathbf{p}}_k \cdot \hat{\mathbf{v}}$, $\hat{\mathbf{p}}_k$ being an eigenvector of $\hat{\mathbf{C}}$. If $\hat{\mathbf{v}}$ is characterized by a covariance matrix, $\hat{\mathbf{\Sigma}}$, then the variance of \hat{w}_k is [33]

$$\text{Var}(\hat{w}_k) = \hat{\mathbf{p}}_k \cdot \hat{\mathbf{\Sigma}} \hat{\mathbf{p}}_k = \text{Tr}(\hat{\mathbf{p}}_k \otimes \hat{\mathbf{p}}_k \cdot \hat{\mathbf{\Sigma}}),$$

and T_n is readily calculated as

$$T_n = \langle |\mathbf{E}|^2 \rangle_n = \frac{2}{n} \text{Var}(\hat{w}_1 + \hat{w}_2) = \text{Tr}(\hat{\mathbf{C}} \hat{\mathbf{\Sigma}}). \quad (16)$$

Note we have used $\hat{\mathbf{C}} = \frac{2}{n} (\hat{\mathbf{p}}_1 \otimes \hat{\mathbf{p}}_1 + \hat{\mathbf{p}}_2 \otimes \hat{\mathbf{p}}_2)$. Here and after and as a good approximation, we assume $\hat{\mathbf{v}}$ has a zero mean. Equation (16) is a *precise* expression to compute T_n given $\hat{\mathbf{\Sigma}}$, and is used to generate the theoretical predictions in Fig. 3b, main panel. The tessellation average T can be computed by taking the weighted sum of T_n , namely, $T = \sum_n (N_n T_n) / \sum_n N_n$, where N_n is the number of n -gons. On the other

hand, sub-ensemble temperatures are typically quantitatively similar to the tessellation temperature, as shown in Fig. 3b inset.

If we further assume that $\hat{w}_{1,2}$ follow identical normal distributions, immediately we have

$$\rho_{\mathbf{E}}(|\mathbf{E}|^2) = \frac{1}{T_n} \exp\left(-\frac{|\mathbf{E}|^2}{T_n}\right). \quad (17)$$

In other words, the exponential distribution arises actually as a χ^2 -distribution with 2 degrees of freedom. On the other hand, if the variances $\text{Var}(\hat{w}_{1,2})$ are not identical but quantitatively similar, which is true for all tessellations we study (see Fig. S5), Eq. (17) still holds to the leading order. (This point is straightforward to prove via Taylor expansion and not shown here for brevity.) Note that even in this situation, per (16) the formula for T_n is still accurate without approximation. This provides an essential illustration of the origin of the E^2 distribution, and Eq. (17) is a main result of the current work. It remains to be shown below that $\hat{w}_{1,2}$ distributions are indeed approximately normal and independent.

Asymptotic normality contributes to statistical regularity

Fig. 4a presents $\hat{w}_{1,2}$ in the hexagon sub-ensemble ($n = 6$) for all 99 tessellations, whereas the cases for $n = 5$ and 7 are included in the SI. PDFs are all normalized for comparison with standard Gaussian, $N(0, 1)$ (dark solid lines). Although the PDFs exhibit appreciable fluctuations due to the relatively small sample size in the n -sub-ensemble, the approximate normalities are evident. Quantitative similarities of $\hat{w}_{1,2}$ are demonstrated in Fig. S5. In addition, $\hat{w}_{1,2}$ are indeed only weakly dependent, as $\text{Cov}(\hat{w}_1, \hat{w}_2)/\text{Var}(\hat{w}_1) = 0.078 \pm 0.046$ for all cases, consistent with the anticipated 2 degrees of freedom. All E^2 distributions (normalized by the predicted temperature T_n) are shown in Fig. 4b.

The apparent candidate to explain the resulting normality is the central limit theorem in the generalized version for dependent and identical random variables [39], noting that \hat{w}_k derives from \hat{v}_k via a linear combination (15). It is peculiar to note that \hat{u}_k and \hat{v}_k themselves also demonstrate approximate normality, shown in Fig. 4c and d. The normality in \hat{u}_k is again explained by the central limit theorem. We can write $\hat{\mathbf{u}}$, the concatenated vector for \mathbf{u}_j 's as (SI)

$$\hat{\mathbf{u}} = \hat{\mathbf{R}}(\hat{\mathbf{y}} - \langle \hat{\mathbf{y}} \rangle), \quad \hat{\mathbf{R}} := \hat{\mathbf{I}} - \frac{1}{n} \hat{\mathbf{e}} \otimes \hat{\mathbf{e}}.$$

In the absence of apparent anisotropy, components of $\hat{\mathbf{y}} - \langle \hat{\mathbf{y}} \rangle$ are approximately dependent yet identical, satisfying precondition of the theorem. Hence \hat{u}_k asymptotes to normality. On the other hand, from Eq. (7) we have $\hat{\mathbf{v}} = \hat{\mathbf{u}}/r_0$ and $r_0 = (\hat{\mathbf{y}} \cdot \hat{\mathbf{e}})/n$. The normality in $\hat{\mathbf{v}}$ is difficult to theoretically prove. However, it is reasonable to speculate the loss of the apparent scale would create similarity to preserve or even enhance normality - see also Figs 4f, g below. In addition, it is extensively confirmed by the data as shown in Fig. 4d.

The asymptotic normality can be better illustrated via a simple Monte Carlo simulation following the schematic in Fig. 1k, where we temporarily restrict to an isolated hexagon, and displacements $\hat{u}_{k,0}$ ($k = 1, 2, \dots, 2n$) are prescribed according to independent, identical distributions as shown in Fig. 4e (Methods, Eqs. (22, 23)). Two representative cases are examined, the first with a steeper than Gaussian initial descent, and the second non-monotonic. In Figs. 4f and g, both \hat{u}_k and \hat{v}_k already demonstrate

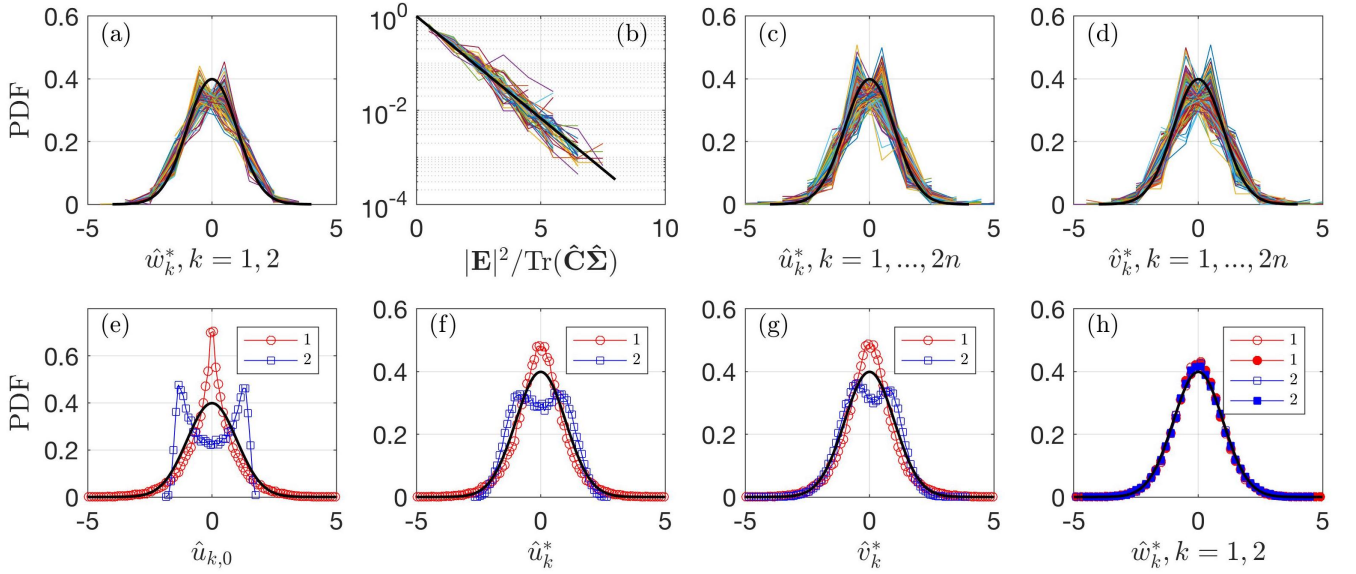


Figure 4: Normality of key variables. Here the superscript $*$ denotes normalization by its own standard deviation so as to compare with $N(0, 1)$, the dark line in all panels except for (b) where it represents an exponential function, $\exp(\cdot)$. (a) PDF for \hat{w}_k^* , $k = 1, 2$, from all tessellations (198 profiles). (b) Normalized $|\mathbf{E}|^2$ follows a simple exponential distribution (99 profiles). (c) and (d) demonstrate the normality of \hat{u}_k and \hat{v}_k ($k = 1, \dots, 2n$) in the hexagon sub-ensemble ($n = 6$), 1188 profiles each. (e) Initial displacement distributions for two exemplary cases, 1 and 2. (f) and (g) \hat{u}_k and \hat{v}_k asymptote toward normality. (g) Normalities of \hat{w}_1 and \hat{w}_2 are well-established.

trending toward normality, although some differences from $N(0, 1)$ are still visible. Note only an arbitrary index k is shown as these distributions are expected to be identical. Subsequently, in Fig. 4h the normality of $\hat{w}_{1,2}$ are well established. $|\mathbf{E}|^2$ distribution quantitatively follows our theoretical prediction and is not shown for brevity. Although only two exemplary tests are presented, repeated simulations reveal the same asymptotic trend to normality and the quantitative relationships (16, 17) always hold.

In a summary, the above exercises demonstrate that asymptotic normality is prevalent in planar tessellations, as key variables derive from linear combinations of statistically similar components. As a result \mathbf{E}^2 distributions become highly regular due to combined normality and its low-dimensionality.

Physical Implications

The physical meaning of \mathbf{E} is self-evident: it represents deformation, and hence is typically associated with energy in one form or another. In the wide range of phenomena we studied, the constitutive relations come in different forms (some are yet unknown). However, some usual possibilities can be contemplated. If the energy is bulk-elastic in nature, then any physically reasonable elastic model of a polygon, valid in the small-to-moderate deformation regime, *must* follow the form [25]

$$\Delta\Psi = \mu|\mathbf{E}|^2, \quad (18)$$

where μ is the first Lamé constant, whereas the second constant is not needed as $\text{Tr}\mathbf{E} = 0$ (SI). On the other hand, if energy is associated with edge lengths or perimeters, such as in the case of models for 2D confluent tissues [7, 34, 44], Eq. (18) is still a formally valid approximation, as the change in perimeter is

also proportional to $|\mathbf{E}|^2$ to leading-order approximation (SI). Last but not least, in the Quantizer problem [15, 27, 36] the cell-wise energy functional is the moment of inertia, which is

$$\text{Tr}\mathbf{M} = 2m_0(1 + |\mathbf{E}|^2) \quad (19)$$

in both two and three dimensions (SI), and $2m_0$ is the moment of inertia of the regular reference polygon, \mathcal{P}_R . Thus its distribution can be computed via knowing both the area and E^2 distributions. These examples of constitutive relations cover a reasonably wide range of physical systems.

Above we have taken the liberty in naming a pseudo-temperature, T (or T_n for the sub-ensembles). Indeed, such definition is both tempting and appropriate in the presence of a Boltzmann-like distribution. The tests by Dean and Lefèvre [13] and McNamara *et al.* [47] become trivial: the ratio of two overlapping exponential distributions will necessarily give another exponential distribution. We therefore name this pseudo-temperature the “ E^2 temperature”, and propose it as a candidate for a thermodynamically meaningful temperature owing to its consistent regularity and connection with physical quantities. This temperature quantifies the overall deformation, and possibly also system energy. To further explore a thermodynamic framework would require system-specific physical principles, e.g., energy minimization, which we shall explore in future work.

We have thus demonstrated three main points in this work: *i*) An exponential distribution in E^2 leads to a k -Gamma distribution in the aspect ratio. In fact, k -Gamma distributions are mere approximations to the more basic solution we develop. *ii*) E^2 distribution is a χ^2 -distribution with two degrees of freedom, arising from combined effects of asymptotic normality and the small dimensionality of \mathbf{E} , which is analogous to the small dimensionality of the volume function in granular assembly [8]. We have developed a formula to compute E^2 from vertex statistics. *iii*) E^2 and aspect ratio distributions as well as normality in displacements are true universal features as we have shown via both a large collection of data and theoretical derivations illustrating their mechanistic origins. The strong regularity in E^2 and vertex displacements are “hidden patterns” revealed by this work. The mean-field strain tensor, with its clear physical and geometric meaning, is an ideal quantity connecting the conservation principles, the energy (or pseudo-energy) landscape, and the geometric distributions. It is a powerful quantifier to describe polygonal networks randomized by active agitations, structural defects, and noises, among others. Analysis may also be extended to polytopes in three and higher dimensions.

Author contributions

HL, LL, and KDI designed the research; HL, LL, RL, and SM developed the theory; RL, ZZ, and CI analyzed images; HL, RL, and SM analyzed data; CI and ZZ performed experiments; HL, LL, and KDI wrote the paper.

Acknowledgement

The authors are grateful to Dr. Yuanwang Pan for providing fixed wing disc images in the Drosophila group. The authors acknowledge helpful discussions with Dr. Troy Shinbrot, and funding support from NIH R21

CA220202-02 (PI: HL); NSF CMMI 1351561 and DMS 1410273 (PI: LL); and NIH R35 GM131748 (PI: KDI).

Competing interests

The authors declare no competing interests.

Data availability

The datasets generated during and/or analysed during the current study are available from the corresponding authors on reasonable request.

Methods

Data Collection

Among the data groups listed in Table 1, the last 3 (Droso Fix, Droso Live, and MDCK) are generated from this work, whereas other data types are collected from the public domain. They are briefly described below, and the specific images analyzed are identified in the references where possible.

Salt Flat of Uyuni (Salt Flat) All images of the Salar de Uyuni (Bolivia) are from online, or captured from still frames of online videos. Credits are given to identifiable author IDs, and time stamps in videos are provided [20, 21, 23, 45, 48, 51, 65].

Landforms on Mars (Mars) All photos come from the High Resolution Imaging Science Experiment (HiRISE) on board the Mars Reconnaissance Orbiter and are produced by NASA, JPL-CalTech and University of Arizona [40, 43, 55, 56, 57, 66]. The mechanisms of geological pattern formation on Mars are still the subject of active studies, and theories include desiccation [43], thermal contraction [40, 55, 56], and ice sublimation [66]. The image from [57] likely indicates ridges of sand dunes.

Veins on Leaves (Leaves) All images are from online where proper credits are given to website, author, or author ID whichever is identifiable [11, 24, 32, 35, 59, 67]. Species are not identified in photos except for [11], which shows *Ficus lyrata* (Fiddle-Leaf Fig).

Landforms in the Arctic (Arctic) Polygonal landforms in or near the Arctic are mostly ice wedges [2, 5, 41, 52, 61, 62, 70] or tundra [12, 46], whereas patterns in the latter typically corroborate with locations of ice wedges, too.

Supergranulation on Solar Surface (Solar) Supergranulation patterns on the solar surface from observations [6, 10, 14, 26, 29, 64].

Cracked dry earth (Cracks) Land cracks, mostly probably formed due to desiccation. Images are collected from the internet [1, 9, 31, 37, 38, 49, 60, 69, 71].

Drosophila wing disc, fixed (Droso) *Drosophila* were cultured at 25°C. To obtain fixed wing discs at different stages, eggs were laid for 2 to 4h, and larvae were dissected at 72, 84, 96, 108 and 120h after egg laying (AEL). Dissected wing discs were fixed in 4% paraformaldehyde for 15 min at room temperature. Staining of fixed wing discs was performed essentially as described in [58] using rat anti-E-cad (1:400 DCAD2; DSHB) and anti-rat Alexa Fluor 647 (Jackson ImmunoResearch, 712-605-153). Images were captured on a Leica SP8 confocal microscope. To compensate for aberrations due to the curvature of wing disc and signals from the peripodial epithelium, we used the Matlab toolbox ImSAnE [28] to detect and isolate a slice of the wing disc epithelium surrounding the adherens junctions, which was then projected into a flat plane, as described previously [53].

Drosophila wing disc, live (Droso) For live imaging of cultured wing discs, larvae expressing GFP-labelled E-cadherin from a Ubi-Ecad:GFP transgene were dissected at 96h AEL, and then cultured based on the procedure of Dye *et al.* [16]. Live wing discs were imaged using a Perkin Elmer Ultraview spinning disc confocal microscope every 8 mins for 12 hours.

Plated MDCKIIG cells (MDCK) MDCKIIG (a gift from W. James Nelson, Stanford University) cells were cultured in low-glucose Dubecco’s modified Eagle’s medium (DMEM) (Life Technologies) supplemented with 10% fetal bovine serum (FBS) and antibiotic-antimycotic. Cells were used at low passage number, checked regularly for contamination by cell morphology and mycoplasma testing. Cells were plated at different densities (1.5, 3, 4.5, 6, and 7.5×10^4 cells/cm²) on coverslips coated with 0.6 mg/ml of collagen for 15 min at room temperature and washed with PBS. After 48 hours, cells were fixed with 4% paraformaldehyde in PBS++ (phosphate- buffered saline supplemented with 100 mM MgCl₂ and 50 mM CaCl₂) for 10 min at room temperature. Immunostaining was performed as in Ibar *et al.* using mouse anti-ZO1 (1:1000, Life Technologies #33-9100) and anti-mouse Alexa Fluor 647 (Jackson ImmunoResearch) [30]. Images were acquired using LAS X software on a Leica TCS SP8 confocal microscope system using a HC PL APO 63×/1.40 objective.

Image and data analysis

Fluorescent images are analyzed using Tissue Analyzer, a plug-in of ImageJ (version 1.52j), from which the cells are sectioned and cell centroids, edges, and vertices are identified. Post-processing is then performed with MATLAB. For each cell, the second area moment tensor, defined with respect to the cell centroid \mathbf{c} , is

$$\mathbf{M} = \int_{\mathcal{P}} (\mathbf{y} - \mathbf{c}) \otimes (\mathbf{y} - \mathbf{c}) dA, \quad (20)$$

where the integration is over the polygon (cell) \mathcal{P} . Note that here we ignore the curvature of cell edges and assume (by approximation) that they are straight lines connecting vertices. Standard and exact formulae are available for polygons which we use to compute the components of \mathbf{M} with only the coordinates of the vertices, \mathbf{y}_j ’s. The aspect ratio a_r is

$$a_r = \sqrt{\frac{\max(\lambda_1, \lambda_2)}{\min(\lambda_1, \lambda_2)}},$$

where λ_1 and λ_2 are eigenvalues of \mathbf{M} .

As an alternative approach to calculate \mathbf{E} , we could bypass \mathbf{F} and make use of the moment. We denote this definition \mathbf{E}_M ,

$$\mathbf{E}_M = \left(\frac{\mathbf{M}}{\sqrt{\det \mathbf{M}}} \right)^{\frac{1}{2}} - \mathbf{I}. \quad (21)$$

In the SI we demonstrate that to the leading order the two definitions are approximately equal. We note that while (21) is an area-based calculation, (5) in the proper text is vertex-based.

The coefficient of determination, R^2 , follows the standard definition,

$$R^2 = 1 - \frac{\text{Var}(\mathbf{f} - \mathbf{f}')}{\text{Var}(\mathbf{f})}.$$

Here 'Var' denotes variance, \mathbf{f} is the data presented in array form, and \mathbf{f}' is the corresponding array generated via fitting (such as for $|\mathbf{E}|^2$) or a theoretical prediction (such as for a_r).

Monte Carlo simulation

Results shown in Fig. 4e-h are generated via a simple Monte Carlo simulation. We generate deformation from regular hexagons using Eq. (2). The initial displacements \mathbf{u}_i^0 follow independent and identical distributions

$$\mathbf{u}_{i,0} = (d_i \cos \theta_i, d_i \sin \theta_i), \quad (22)$$

where θ_j is uniformly distributed between $[0, 2\pi]$, and d_i follows

$$d_i \sim \beta p d_i^{p-1} \exp(-\beta d_i^p). \quad (23)$$

We set β to ensure the variances of the components are 1. The exponent $p = 4/3$ gives test case 1 (red) shown in Fig. 4e, whereas $p = 10$ gives test case 2 (blue), which has a non-monotonic distribution of d_i , and hence $\hat{u}_{k,0}$. These random initial displacements lead to a centroid-translation (SI),

$$\mathbf{c} = \frac{1}{n} \sum_{i=1}^n \mathbf{u}_{i,0}.$$

Center-correction of $\mathbf{u}_{i,0}$ provides \mathbf{u}_i and \mathbf{y}_i in (2). Once \mathbf{y}_i 's are generated, other quantities such as \hat{v}_i , \hat{w}_i and $|\mathbf{E}|^2$ are computed according to formula provided in the proper text.

References

- [1] 3dshtamp (author ID). Online image: White or light gray brick texture. [URL: <https://www.shutterstock.com/image-illustration/white-light-gray-brick-texture-765044275>].
- [2] The International Permafrost Association. Online image: Permafrost polygon. [URL: <https://ipa.arcticportal.org/products/mediamenu/galleries/category/1-permafrost-impressions>].
- [3] L. Atia, D. Bi, Y. Sharma, J. A. Mitchel, B. Gweon, S. A. Koehler, S. J. DeCamp, B. Lan, J. H. Kim, R. Hirsch, A. F. Pegoraro, K. H. Lee, J. R. Starr, D. A. Weitz, A. C. Martin, J.-A. Park, J. P. Butler, and J. J. Fredberg. Geometrical constraints during epithelial jamming. *Nat. Phys.*, 14:613–620, 2018.
- [4] D. Barthès-Biesel and H. Sgaier. Role of membrane viscosity in the orientation and deformation of a spherical capsule suspended in simple shear flow. *J. Fluid Mech.*, 160:119–135, 1985.
- [5] C. Bernard-Grand’Maison and W. Pollard. An estimate of ice wedge volume for a High Arctic polar desert environment, Fosheim Peninsula, Ellesmere Island, figure 4 top right panel. *Cryosphere*, 12(11):3589–3604, 2018.
- [6] F. Berrilli, I. Ermolli, A. Florio, and E. Pietropaolo. Average properties and temporal variations of the geometry of solar network cells, figure 1 right panel. *Astron. Astrophys.*, 344:965–972, 1999.
- [7] D. Bi, J. H. Lopez, J. M. Schwarz, and M. L. Manning. A density-independent rigidity transition in biological tissues. *Nat. Phys.*, 11:1074–1079, 2015.
- [8] R. Blumenfeld and S. F. Edwards. Granular entropy: Explicit calculations for planar assemblies. *Phys. Rev. Lett.*, 90(11):114303, 2003.
- [9] calling wisdom (author ID). Online image: Cracked land, June 2009. [URL: <http://www.nipic.com/show/2/8/ee5e32f449b1c4e7.html>].
- [10] S. Chatterjee, S. Mandal, and D. Banerjee. Variation of supergranule parameters with solar cycles: Results from century-long Kodaikanal digitized Ca II K data, figure 1(d). *Astrophys. J.*, 841(2):70 (10pp), 2017.
- [11] D. Clode. Online image: *Ficus lyrata* leaf, October 2012. [URL: <https://reforestation.me/flower-photos-1/>].
- [12] F. Cresto-Aleina. *Scale interactions in high-latitude ecosystems*, figure 2.1. PhD thesis, Max Planck Institute for Meteorology, 2014.
- [13] D. S. Dean and A. Lefèvre. Possible test of the thermodynamic approach to granular media. *Phys. Rev. Lett.*, 90(19):198301, 2003.
- [14] M. L. DeRosa and J. Toomre. Evolution of solar supergranulation, figure 7(a). *Astrophys. J.*, 616(2):1242–1260, 2004.
- [15] Q. Du and D. Wang. The optimal centroidal voronoi tessellations and the Gershó’s conjecture in the three-dimensional space. *Computer and Mathematics with Applications*, 49(9-10):1355–1373, 2005.

- [16] N. A. Dye, M. Popović, S. Spannll, R. Etournay, D. KainmÄCeller, S. Ghosh, E. W. Myers, F. JÄElicher, and S. Eaton. Cell dynamics underlying oriented growth of the drosophila wing imaginal disc. *Development*, 144:4406–4421, 2017.
- [17] S. F. Edwards and D. V. Grinev. Statistical mechanics of vibration-induced compaction of powders. *Phys. Rev. E*, 58:4758, 1998.
- [18] S. F. Edwards and R. B. S. Oakeshott. Theory of powders. *Physica A*, 157:1080–1090, 1989.
- [19] R. Farhadifar, J. Röper, B. Aigouy, S. Eaton, and F. Jülicher. The influence of cell mechanics, cell-cell interactions, and proliferation on epithelial packing. *Curr. Biol.*, 17:2095–2104, 2007.
- [20] Fly around the world (author ID). Online video: Travel the world, Uyuni vol1, Bolivia by drone (Phantom), t=101 s, February 2016. [URL: <https://www.youtube.com/watch?v=GSYLH462Nis>].
- [21] Flying The Nest (author ID). Online video: Bolivia salt flats, Salar de Uyuni, worlds largest mirror, t=493 s, November 2017. [URL: https://www.youtube.com/watch?v=V_RFDqrJC9U&t=493s].
- [22] S. Garcia, E. Hannezo, J. Elgeti, J.-F. Joanny, P. Silberzan, and N. S. Gov. Physics of active jamming during collective cellular motion in a monolayer. *Proc. Natl. Acad. Sci. USA*, 112:15314–15319, 2015.
- [23] gflandre (author ID). Online image: Salar de Uyuni, February 2018. [URL: <http://www.dronestagr.am/salar-de-uyuni/>].
- [24] gitan100 (author ID). Online image: Vector leaf veins seamless texture. [URL: <https://www.shutterstock.com/zh/image-vector/vector-leaf-veins-seamless-texture-98150471?src=HUAi-C5Hv27glBnNFx2Y4Q-1-41>].
- [25] M. E. Gurtin, E. Fried, and L. Anand. *The Mechanics and Thermodynamics of Continua*. Cambridge University Press, 2010.
- [26] H. J. Hagenaar and C. J. Schrijver. The distribution of cell sizes of the solar chromospheric network, figure 3 lower panel. *Astrophys. J.*, 481(2):988–995, 1997.
- [27] T. M. Hain, M. A. Klatt, and G. E. Schröder-Turk. Low-temperature statistical mechanics of the QuanTizer problem: fast quenching and equilibrium cooling of the three-dimensional Voronoi liquid. *arXiv*, 2020.
- [28] I. Heemskerk and S. J. Streichan. Tissue cartography: compressing bio-image data by dimensional reduction. *Nat. Methods*, 12:1139–1142, 2015.
- [29] J. Hirzberger, L. Gizon, S. K. Solanki, and T. L. Duvall. Structure and evolution of supergranulation from local helioseismology, figure 7. In L. Gizon, P. S. Cally, and J. Leibacher, editors, *Helioseismology, asteroseismology and MHD connections*, pages 415–435. Springer, New York, 2008.
- [30] C. Ibar, E. Kirichenko, B. Keepers, E. Enners, K. Fleisch, and K. D. Irvine. Tension-dependent regulation of mammalian Hippo signaling through LIMD1. *J. Cell Sci.*, 131(5):jcs214700, 2018.

- [31] Inspired Boy (author ID). Online image: Surface crack material [PSD], October 2015. [URL: <http://inspiredboy.com/surface-crack-material/>].
- [32] J. W. Kimball. Online image: The leaf, January 2012. [URL: <http://www.biology-pages.info/L/Leaf.html>].
- [33] R. A. Johnson and D. W. Wichern. *Applied Multivariate Statistical Analysis*. Pearson Prentice Hall, 6th edition, 2007. p. 76.
- [34] S. Kim and S. Hilgenfeldt. Cell shapes and patterns as quantitative indicators of tissue stress in the plant epidermis. *Soft Matter*, 11:7270–7275, 2015.
- [35] N. Kinnear. Online image: Leaf lines V, September 2011. [URL: <https://fineartamerica.com/featured/leaf-lines-v-natalie-kinnear.html>].
- [36] M. A. Klatt, J. Lovrić, D. Chen, S. C. Kapfer, F. M. Schaller, P. W. A. Schönhöfer, B. S. Gardiner, A.-S. Smith, G. E. Schröder-Turk, and S. Torquato. Universal hidden order in amorphous cellular geometries. *Nature Communications*, 2019.
- [37] Kojihirano (author ID). Online image: Dry lake bed texture. [URL: <https://www.dreamstime.com/stock-photo-dry-lake-bed-texture-crackled-earth-racetrack-death-valley-national-park-california-image41139404>].
- [38] kzww (author ID). Online image: Cracked dry earth. [URL: <https://www.shutterstock.com/image-photo/cracked-dry-earth-abstract-background-1142812457>].
- [39] E. L. Lehmann. *Elements of Large-Sample Theory*. Springer, 1999.
- [40] J. Levy, J. Head, and D. Marchant. Thermal contraction crack polygons on Mars: Classification, distribution, and climate implications from HiRISE observations, figure 2(b), 7(b), 8(a) and (b). *J. Geophys. Res. Planets*, 114(E1), 2009.
- [41] A. K. Liljedahl, J. Boike, R. P. Daanen, A. N. Fedorov, G. V. Frost, G. Grosse, L. D. Hinzman, Y. Iijma, J. C. Jorgenson, N. Matveyeva, M. Necsoiu, M. K. Reynolds, V. E. Romanovsky, J. Schulla, K. D. Tape, D. A. Walker, C. J. Wilson, H. Yabuki, and D. Zona. Pan-Arctic ice-wedge degradation in warming permafrost and its influence on tundra hydrology, figure 3(a) and (b), middle panel. *Nat. Geosci.*, 9(1):312–318, 2016.
- [42] A. J. Liu and S. R. Nagel. Jamming is not just cool any more. *Nature*, 396:21–22, 1998.
- [43] M. R. El Maarry, W. J. Markiewicz, M. T. Mellon, W. Goetz, J. M. Dohm, and A. Pack. Crater floor polygons: Desiccation patterns of ancient lakes on Mars, figure 12 right panel. *J. Geophys. Res. Planets*, 115(E10), 2010.
- [44] M. L. Manning, R. A. Foty, M. S. Steinberg, and E.-M. Schoetz. Coaction of intercellular adhesion and cortical tension specifies tissue surface tension. *Proc. Natl. Acad. Sci. USA*, 107(28):12517–12522, 2010.

- [45] J. Martinez. Online video: Trailer San Pedro - Uyuni 2017 drone view, t=23 s, September 2017. [URL: <https://www.youtube.com/watch?v=tqX3dYHGF8g&t=23s>].
- [46] N. Matt. Online image: Science in the 1002 area. Fodar News, February 2019. [URL: <http://fairbanksfodar.com/science-in-the-1002-area>].
- [47] S. McNamara, P. Richard, S. Kiesgen de Richter, G. Le Caër, and R. Delannay. Measurement of granular entropy. *Phys. Rev. E*, 80(3):031301, 3009.
- [48] Mika world tour (author ID). Online video: Voyage au Salar de Uyuni, t=127s, January 2017. [URL: <https://www.youtube.com/watch?v=u291MNVpRlM&t=127s>].
- [49] T. Mongkolsin. Online image: Soil texture crack background. [URL: https://www.123rf.com/photo_31964240_soil-texture-crack-background.html?fromid=VTRRbHHQW1qWVRmbzFYWEwxSjZxUT09].
- [50] K. D. Nnetu, M. Knorr, S. Pawlizak, T. Fuhs, and J. A. Kas. Slow and anomalous dynamics of an MCF-10A epithelial cell monolayer. *Soft Matter*, 9:9335–9341, 2013.
- [51] North Branch (author ID). Online video: Uyuni salt flats (Salar de Uyuni) drone, Potosi - Bolivia, t=85 s, September 2017. [URL: <https://www.youtube.com/watch?v=CbVGic9GQR4&t=85s>].
- [52] The Arctic Research Consortium of the United States. Online image: Landscape change in the tundra: Citizen-scientist driven arctic observations, 2018. [URL: <https://www.arcus.org/tac/projects/landscape-change>].
- [53] Y. Pan, I. Heemskerk, C. Ibar, B. I. Shraiman, and K. D. Irvine. Differential growth triggers mechanical feedback that elevates Hippo signaling. *Proc. Natl. Acad. Sci. USA*, 113:E6974–E6983, 2016.
- [54] J.-A. Park, J. H. Kim, D. Bi, J. A. Mitchel, N. T. Qazvini, K. Tantisira, C. Y. Park, M. McGill, S.-H. Kim, B. Gweon, J. Notbohm, R. Steward Jr, S. Burger, S. H. Randell, A. T. Kho, D. T. Tambe, C. Hardin, S. A. Shore, E. Israel, D. A. Weitz, D. J. Tschumperlin, E. P. Henske, S. T. Weiss, M. L. Manning, J. P. Butler, J. M. Drazen, and J. J. Fredberg. Jamming and cell shape in the asthmatic airway epithelium. *Nat. Mater.*, 14:1040–1048, 2015.
- [55] The HiRISE Project. Online image: Polygonal patterned ground, February 2010. [URL: https://www.uahirise.org/ESP_016641_2500].
- [56] The HiRISE Project. Online image: Polygonal patterned ground, April 2012. [URL: <https://mars.nasa.gov/resources/5314/polygonal-patterned-ground/>].
- [57] The HiRISE Project. Online image: Polygonal dunes, May 2013. [URL: <https://photojournal.jpl.nasa.gov/catalog/PIA17726>].
- [58] C. Rauskolb and K. D. Irvine. Localization of Hippo signaling components in *Drosophila* by fluorescence and immunofluorescence. In A. Hergovich, editor, *Methods in Molecular Biology, Vol. 1893: The Hippo pathway*, pages 61–73. Humana Press, 2018.

- [59] rclassenlayouts (author ID). Online image: Leaf vein. [URL: https://www.123rf.com/photo_19683272_leaf-vein-veins-branched-network-photosynthesis-spring-green-leaf-surface-texture.html].
- [60] Releon8211 (author ID). Online image: Dried and cracked ground. [URL: <https://www.dreamstime.com/stock-photo-dried-cracked-ground-general-illustration-image56453384>].
- [61] D. Ronald. Online image: High centered orthogonal ice wedge polygons in northern Canadian archipelago, November 2009. [URL: <http://permafrost.gi.alaska.edu/photos/image/80>].
- [62] S. Matthew. Online image: Ivotuk polygons. [URL: <https://www.erd.usace.army.mil/Media/Images/igphoto/2000725201/>].
- [63] M. Sadati, N. T. Qazvini, R. Krishnan, C. Y. Park, and J. J. Fredberg. Collective cell migration and cell jamming. *Differentiation*, 86(3):121–125, 2013.
- [64] C. J. Schrijver and H. J. Hagenaar. On the patterns of the solar granulation and supergranulation, figure 2. *Astrophys. J.*, 475(1):328–337, 1997.
- [65] Sergeo540 (author ID). Online video: Bolivia Sucre Salar de Uyuni cinematic travel video 4K, t=163 s, January 2019. [URL: <https://www.youtube.com/watch?v=Ha7twopCwHw&t=163s>].
- [66] R. J. Soare, S. J. Conway, L. E. McKeown, E. Godin, and J. Hawksell. Possible ice-wedge polygons in Utopia Planitia, Mars, and their poleward latitudinal-gradient, figure 4. In *50th Lunar and Planetary Science Conference*, volume 50, March 2019.
- [67] SuradechK (author ID). Online image: Leaf-texture abstract background with closeup view on leaf veins. [URL: <https://www.canstockphoto.ca/leaf-texture-abstract-background-with-38163721.html>].
- [68] V. Trappe, V. Prasad, L. Cipelletti, P. N. Segre, and D. A. Weitz. Jamming phase diagram for attractive particles. *Nature*, 411:772–775, 2001.
- [69] Y. Wang, D. Feng, and C. W. Ng. Modeling the 3D crack network and anisotropic permeability of saturated cracked soil, figure 1. *Comput. Geotech.*, 52:63–70, 2013.
- [70] P. Worsley. Ice-wedge growth and casting in a Late Pleistocene periglacial, fluvial succession at Baston, Lincolnshire, figure 5. *Mercian Geol.*, 18(3):159–170, 2014.
- [71] Zhaojiankang (author ID). Online image: Tierra secada y agrietada. [URL: <https://es.dreamstime.com/imagen-de-archivo-libre-de-regal%C3%ADas-tierra-secada-y-agrietada-image39145796>].